

Origin of slow earthquake statistics in low-friction soft granular shear

Yuto Sasaki^{1*}, Hiroaki Katsuragi¹

¹Department of Earth and Space Science, University of Osaka.

*Corresponding author. Email: sasaki.geoscience@gmail.com

Slow earthquakes differ from regular earthquakes in their slower moment release and limited size distribution. What mechanisms cause slow earthquakes that manifest these unique statistics? We experimentally demonstrate that their characteristics emerge from low-friction soft granular shear. Using a hydrogel particle layer floated on lubricating fluid, we conducted stick-slip experiments. The observed slip events follow the same laws of both moment release rate and size distribution as slow earthquakes, contrasting with frictional rigid granular shear. Slip size is determined by the competing effects of shear localization and pressure enhancement with decreasing porosity. These findings indicate that low friction and particle softness in sheared granular systems with monotonous structures cause slow earthquake statistics, which may monitor pore fluid dynamics and shear localization within hazardous fault zones.

Slow earthquakes are distinctively slower slip phenomena than regular earthquakes of equivalent size (1, 2). Between slow and regular earthquakes, the statistics of seismic moment release rate (1, 2) and moment-frequency distribution (3, 4) often exhibit different characteristics. Nevertheless, the mechanisms responsible for the distinct faulting processes of slow earthquakes remain controversial. To explain the long-lasting dynamics of slow earthquakes, numerous observations suggest the crucial role of viscous fluid around faults (5–10). Additionally, some theoretical explanations

propose the effect of diffusional dynamics of fault size evolution (11). However, the origin of multiple unique statistical laws of slow earthquakes has rarely been investigated through experiments, owing to two main difficulties: reproducing the observed statistics within finite system sizes, and directly observing materials' internal microstructures during rock deformation testing. Experimental elucidation of their enigmatic origin would bridge the difference between slow and associated devastating earthquakes underground (2, 12), which control the energy balance of plate tectonics.

In this study, we conducted quasi-two-dimensional rotary shear experiments on a low-friction hydrogel granular layer floating on a viscous lubricating liquid surface and measured mechanical torque (Fig. 1A) [see (13) for details]. The experimental system enables the systematic variation of the bulk porosity ϕ and direct tracking of particle motion (Fig. 1B), both of which intrinsically govern the behavior of fluid-retaining faults. We captured hundreds of stick and slow-slip events, which become more pronounced with decreasing porosity (Fig. 1C, D). Slip events in this low-friction, soft granular system simultaneously follow two statistical characteristics of slow earthquakes: the moment-duration scaling and moment-frequency distribution (2, 3), as shown in Fig. 2. Based on the in situ particle observation, shear localization at lower porosity (Fig. 3) explains these porosity-dependent statistics of slip moment (Fig. 4), as well as the depth distribution of earthquakes across the spectrum of their types (Fig. 5).

Moment statistics of slow earthquakes resulting from fluid-lubricated soft granular slip phenomena

The fluid-lubricated soft granular layer under shear exhibited torque fluctuations corresponding to stick–slip events (Fig. 1C), where precursory slip movements initiate a few seconds before the stress drop (fig. S1). In this lubricated system, the stick-slip behavior involves both partially decoupled stable shear during the stick phase and unstable slip with torque drops, accommodating total displacement similar to that in slow earthquakes (Fig. 1D). At a porosity of $\phi = 0.18$, the unstable slip events accounted for 32% of the total displacement, whereas virtually 0% at $\phi \gtrsim 0.24$. A decrease in porosity to approximately 0.2 caused a transition from steady flow to stick-slip behavior, which exceeded the steady shear rate (Fig. 1C, D). The decrease in porosity causes an increase in both the mean torque strength and its drop amplitude (Fig. 1C, fig. S2A, B), which

are defined in the inset of Fig. 1C. The maximum torque at the minimum porosity is substantially lower than the irrecoverable failure strength of the particle. The porosity dependence of the torque drop amplitude remains consistent across system sizes ranging from 100 to 300 mm in diameter (fig. S2B).

We statistically analyzed the moment M_0 and its rate \dot{M}_0 of the slip events, calculated from the torque drop amplitude, drop duration, and observed slip area (Supplementary Text). Consistent with the variation in the torque drop amplitude (fig. S3A, B), a decrease in porosity from 0.41 to 0.18 progressively increases both the amount and rate of moment release (Fig. 2): the mean moment from 1.3×10^{-10} to 3.8×10^{-9} N m, and the mean rate from 2.4×10^{-10} to 8.2×10^{-10} N m/s. Statistically, the moment M_0 follows an exponential distribution, regardless of porosity (Fig. 2A). This is in contrast with regular earthquakes and dry granular materials, which follow a power-law distribution with an exponent known as the b -value, called the Gutenberg-Richter law (14, 15). However, slow earthquakes frequently follow an exponential distribution or a power-law distribution with a higher b , both of which are difficult to statistically distinguish (3, 4, 16–19). The exponential distribution observed in slow earthquakes represents a scale-limited process characterized by the area and/or amount of slip (3). Moreover, our experiments revealed that the moment M_0 is nearly proportional to the release duration T , indicating a constant moment rate \dot{M}_0 (Fig. 2B). Linear scaling $M_0 \propto T$ has been observed in slow earthquakes (1, 2), contrary to the power scaling $M_0 \propto T^3$ of regular earthquakes (20, 21). The moment rate of slow earthquakes is suggested to have a constant upper bound (2). Our laboratory experiments reliably reproduce these statistical properties of M_0 and \dot{M}_0 as observed in slow earthquakes.

Granular motions resulting in slow earthquake statistics

To investigate the representative particle movements contributing to the observed moment statistics, we captured the in situ particle arrangements as binary images every 0.1 s (Fig. 1B). Fig. 3A–C shows the comparison of the time-lapse images for $\phi = 0.23, 0.20,$ and 0.18 , mapping the standard deviation of temporally varying binary values at each pixel over approximately 1100 s and 660° rotation. These images reveal three types of regions formed at any porosity: the central shear band with active motion (continuous white region), surrounding vibration region with particle drift

shorter than the particle diameter, and outer fixed region with no noticeable motion. The particles principally slip on the boundary plane between the shear band and surrounding vibration region. The shear band becomes more localized at lower porosities. As ϕ decreased from 0.41 to 0.18, the shear band thickness w decreased from $\gtrsim 9d$ to $2d$ with the particle diameter d , and we obtained a linear relationship of $w(\phi)$ (Fig. 4A). Notably, the released moment exhibits larger values under conditions of lower porosity despite the shear localization. Meanwhile, the porosity within the localized shear band remained constant at 0.3 independent of ϕ , which is higher (richer in fluid content) than the bulk, except under the highest ϕ value in run #79 (fig. S2E). The shear band thickness of less than ten particle diameters, which is a typical value for frictional conditions (22), is associated with the shorter correlation length of force chains under low modulus (23) and low friction. This trend is evident in Fig. 3A–C. Additionally, the surrounding vibration region exhibits radial anisotropy that persists throughout the entire run time (Fig. 3A–C). This indicates the presence of fixed force-chain structures (24), which supports the shear band without their significant rearrangement during slip events. Furthermore, the outer fixed region implies that the mechanical correlation length is sufficiently short relative to the entire system size. This ensures that slip and rupture propagation are confined within the shear band, not extending throughout the entire system. The outer fixed region should constrain the shear band thickness w through its pressure, which depends on porosity ϕ .

We further examined the distribution and evolution of slip planes associated with each event. Fig. 3D illustrates the typical types of particle motion with instantaneous displacement at $\phi = 0.20$. The white areas indicate particle differential motion over 2 s. Quantifying the number of these moving particles during each event reveals that slip events predominantly occurred on slip planes of similar size within the shear band for each porosity, independent of the moment M_0 (fig. S4; Supplementary Text). This justifies defining a representative constant value of slip plane area $S(w(\phi))$ for each porosity. Fig. 3E shows the temporal evolution of slip motions over 15.2 s, corresponding to the torque drops. The yellow arrows indicate the rupture front, which is identified as the boundary between areas of particle mobility and the quiescent surroundings. Its propagation timescale is in the range of approximately 1 s. This rupture time is relatively shorter than the overall slip timescale in this lubricated system, making itself negligible compared with the event duration T . Thus, the low-friction and soft granular motion is primarily characterized by shear localization

with decreasing porosity and slip on a plane of constant area for each porosity, regardless of the moment. These unique characteristics of the granular dynamics can explain the moment statistics.

Possible mechanisms consistent with physical and geological observations

The low-friction soft granular system exhibits both the exponential frequency distribution of the moment M_0 and its constant rate \dot{M}_0 (Fig. 2). These two statistical laws remain consistent across various experimental conditions (table S1), including different particle arrangements (ordered polycrystalline structure with monodisperse particles (Fig. 2) and random structure with bidisperse mixtures of the hydrogel particles and half-diameter glass beads), liquid viscosities, and system sizes (fig. S5). This universality ensures that the two statistical laws can be explained by a simple model as follows.

First, the exponential distribution of the moment M_0 (Fig. 2A) should emerge from the strength of the granular layer, which is generally supported by force chains (24, 25). The stress of both force chains and consisting particles follows an exponential distribution (24, 26–28). In contrast to our lubricated system, dry frictional systems under confining pressure follow power-law distributions (29, 30). In the frictional systems, the force chains form networks that can cascade into critical slip avalanches. However, lubrication inhibits the formation of the force chain network and constrains slip size to the individual particle scale, resulting in the suppression of the moment release during slip events, (Fig. 5A–C). Considering that effectively softer systems often exhibit exponential distributions of slip size (31, 32), we investigated the combined effects of lubrication and material softness. When we substituted hydrogel particles with more rigid glass beads with frictional surfaces, we observed a similar exponential distribution under lubrication (fig. S6A). These results demonstrate that low friction (and material softness) play a crucial role in limiting the mechanically correlated length and preventing cascade collapse events. Consequently, low-friction and/or softer systems manifest the moment statistics that reflect the stress distribution of individual force chains (Fig. 5A, B).

The characteristic scale of slip moment distribution can be determined by the balance between the enhanced force chain strength and localized slip area with pressure. To explain the relationship between the mean moment and porosity, we assume that slips occur repeatedly on the outer side wall

of the cylindrical shear band, as shown in the inset of Fig. 4A. The shear band has a thickness w and a diameter δ of the interparticle contact area. The seismic moment is defined as $M_0 = \mu SD$, where μ is the shear modulus, S is the slip area, and D is the slip displacement (33). This moment resulting from the torque drop with an amplitude $\Delta\Gamma$ and associated slip with a plane area $S = 2\pi(R + w)\delta$ can be calculated as,

$$M_0 = \frac{\delta}{C(R + w)}\Delta\Gamma = \frac{2\pi\delta^2}{C}(R + w)\Delta\sigma, \quad (1)$$

with the shear stress drop $\Delta\sigma$, a geometrical constant C , and the cylinder radius R (Supplementary Text). In this equation, the mechanical force drop $\Delta\Gamma/(R + w)$ is converted into the moment on the slip plane with the characteristic width δ . Equation 1 adequately explains the porosity-dependent characteristic moment $\langle M_0 \rangle$, where $\langle \rangle$ denotes the mean value, with the fitted scaling $\langle \Delta\sigma \rangle \propto \phi^{-n}$ ($n = 5.0$), linear relationship $w(\phi)$, and assumption of a constant δ (solid line in Fig. 4B). This indicates that despite shear localization, the increases in pressure and shear stress predominantly control the moment size, which is consistent with the interpretation that the force chain strength governs the moment statistics. Granular materials typically exhibit a rigidity phase transition and pressure enhancement with decreasing porosity (34), which is also observed in this study (fig. S2C). Thus, the moment-frequency distribution is governed by the exponentially distributed stress drop $\Delta\sigma$ and its corresponding slip displacement D , which vary with porosity and associated pressure condition (fig. S3; Supplementary Text).

Second, the linear scaling between moment and duration, $M_0 \propto T$ (Fig. 2B), indicates a violation of self-similarity (fractal) holding in regular earthquakes, where $M_0 \propto T^3$ (20, 21). In regular earthquakes, self-similarity emerges from the relationship between slip area S and displacement D , where larger slip areas require greater displacements as $D \propto \sqrt{S}$. In contrast, our low-friction soft granular system exhibits the opposite trend, where D increases as $S(w(\phi))$ and ϕ decrease (fig. S3C). We observed that the temporally averaged slip velocity of the cylinder $\bar{V} (\propto D/T)$ remains constant regardless of porosity (figs. S2D, S8), resulting in the linear scaling $M_0 \propto \mu S \bar{V} T \propto T$ with constant $S(w(\phi))$ for each porosity (Fig. 4A). The scaling between moment and release duration has been extensively studied in granular and dislocation dynamics (35–39). These studies imply that lower driving rates reduce the exponent of T for the event size, approaching unity. Although the underlying mechanism remains unclear in these studies, an increase in timescale or material relaxation results in a nearly constant moment rate, as demonstrated by our system (fig. S7) and

seismic observations (2). Furthermore, when we investigated the effect of material softness on the scaling using glass beads, a nonlinear scaling of $M_0 \propto T^2$ was observed (fig. S6B). This suggests that the viscoelasticity of particles is related to the constancy of slip area and velocity, which realizes the linear scaling. Rigid particles, such as glass beads and fault grains in the seismogenic zone, preserve the fractality of the contact roughness, resulting in the cubic scaling $M_0 \propto T^3$ (Fig. 5F). In contrast, viscoelastic particles cause more contact area and longer, larger relaxation. This leads to a reduction in the fractality of interparticle contact roughness and slip plane size distribution (fig. S4), resulting in the linear scaling $M_0 \propto T$ (Fig. 5E).

The constant moment rate $\dot{M}_0 (= M_0/T)$ in linear scaling can be expressed in terms of the system's torsional stiffness K (Nm/°) using,

$$T = \bar{D}/\bar{V} = \frac{c\Delta\Gamma/360K\bar{V}}{1 - c\omega/360\bar{V}}, \quad (2)$$

with the tangential slip displacement $\bar{D} = \bar{V}T$, circumference $c = 2\pi R$, and angular velocity ω (°/s) of the cylinder (Supplementary Text). The numerator of this equation represents the elastic shear displacement, whereas the denominator applies a correction for the steady rotation of the motor during each slip. Thus, the moment rate \dot{M}_0 is determined only by the shear band thickness $w(\phi)$ and the constant slip velocity \bar{V} (Equation 1, 2), which is consistent with the constant torque drop rate $\Delta\Gamma/T$ and exponentially distributed slip displacement \bar{D} (fig. S3B, C). This model effectively explains the increase in moment rate with decreasing porosity and shear localization (Fig. 4C). As the shear band thickness has a minimum value of $w \sim d$ in this study, the moment rate should approach a maximum limit (dashed line in Fig. 4C). In natural fault systems, the slip plane thickness for each event typically ranges from 1 mm to 1 cm in the fault core (40). This characteristic length scale of shear localization possibly constrains both the moment scale and maximum moment rate (2) observed in slow earthquakes. Our interpretation using quantitative models for both the exponential distribution and the linear scaling provides a self-consistent framework. This proposes that both low interparticle friction (for the moment-frequency distribution) and particle viscoelasticity (for the moment-duration scaling) suppress the cascading up and fractality of faulting.

New implications to slow earthquake faulting with low friction and softness

This study provides a satisfactory qualitative representation of the geophysically observational results and provide insights into the statistical origins of enigmatic slow earthquakes. Fault zones of slow earthquakes are presumed to be lubricated, with high-pressure (nearly lithostatic) pore fluid causing low effective stress (41, 42), and/or ductile matrix surrounding brittle porphyroclasts (43–45). As slow earthquakes, the moment of lubricated soft granular slips follows an exponential distribution and its rate remains constant, both of which increase with decreasing porosity and shear localization. The results imply that even low-friction systems could generate discontinuous slips and occasionally radiate elastic waves through viscoelastic deformation, without necessarily invoking frictional effects, such as the rate-and-state law (46–48). Such a situation requires discrete interparticle interactions and viscoelastic particle deformation under lubrication, which mitigate the cascading processes and fractality of faulting. Building upon our findings, this simple experimental system can facilitate further promising investigations into the effects of spatial dimension, system scale and geometry, particle size distribution, viscous diffusivity (11), and rupture propagation duration (49).

The porosity dependence of moment statistics can qualitatively explain the spatial distribution of earthquakes through shorter force chain buckling with low friction (25) and shear localization in softer granular materials (23). Fig. 5A–C schematically illustrate the fault cores in the deeper region on the downdip transition zone, in the shallower region on the same zone, and in the seismogenic zone, respectively (Fig. 5D). Our results suggest that with much fluid or ductile matrix at higher porosity, the internal shear band is supported by force chains comprising the surrounding shear zone (Fig. 5A). The reduction in porosity and localization of the internal shear band facilitate the formation of force chain networks within the shear zone, which governs the macroscopic slip avalanche behavior (Fig. 5C). As shown in Fig. 5B, the distribution of longer-term slow slip events in the shallower region on the transition zone, adjacent to the seismogenic zone (50), might be explained by lower porosity with longer and slightly faster slip than in the deeper region (Fig. 2B, fig. S8).

From the experimental insights, an exponential distribution of the seismic moment can be expected in regions with significantly high pore pressure and low effective friction. It is anticipated to

discover some geological evidence indicating no frictional slip or plugging but rather granular force chain buckling associated with jamming (51, 52). Moreover, the constant moment rate of slow earthquakes potentially reflects shear localization controlled by porosity, which could critically induce or evolve faster, regular earthquakes. Therefore, temporal observations of the statistical distribution of the seismic moment and moment rate have possibly detected changes in the amount of lubricating pore fluid and strength of hydrated fault gouge, respectively. Spatiotemporal observations of slow earthquakes could help monitor fluid-driven rupture propagation, stress concentration, and fault weakening around seismogenic zones, potentially inducing regular earthquakes and devastating seismic hazards, such as the 2024 M_w 7.5 Noto earthquake (53).

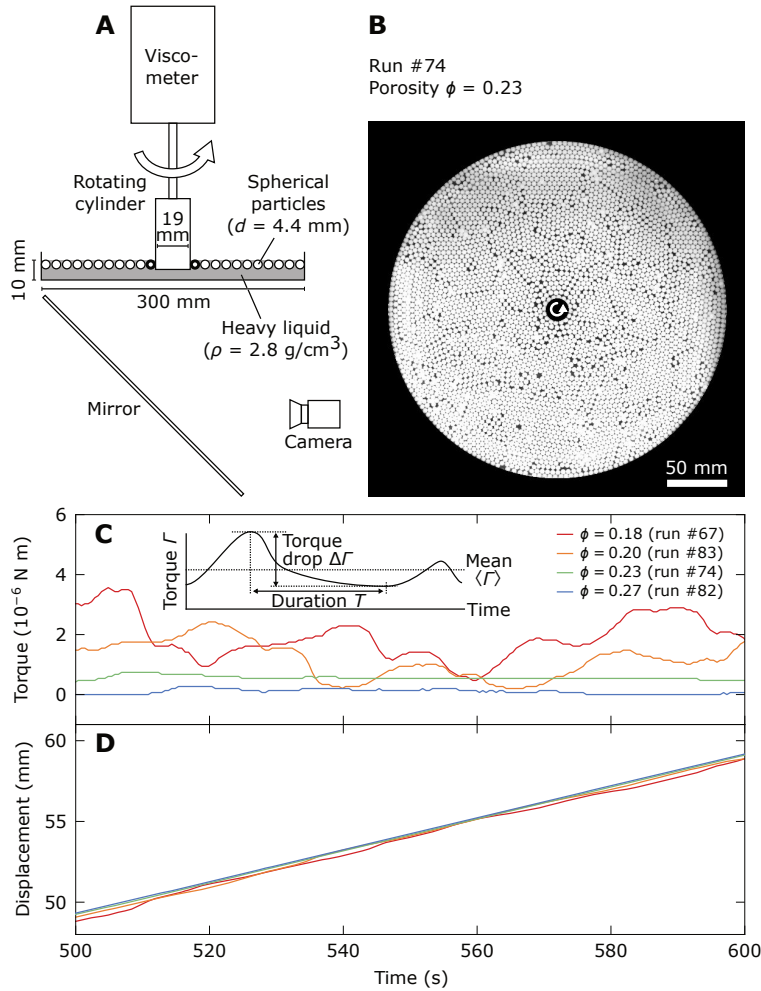


Figure 1: Experimental setup and observed stick-slip behavior. (A) Quasi-two-dimensional granular shear apparatus. Spherical gel particles (4.4 mm in diameter) are floated on a heavy liquid (2.8 g/cm^3). A cylinder, coupled to a viscometer motor through a torsion spring, rotates at a constant angular velocity of $0.6^\circ/\text{s}$. 16 particles (indicated by thick circles) are fixed to the cylinder surface. Particle motions were tracked in situ from the bottom of the container. The floating particle layer (300 mm in diameter) is penetrated by the rotating cylinder (18.84 mm in diameter) in a 10 mm thick liquid layer. The schematic of the figure is not drawn to scale. (B) Representative image at a porosity ϕ of 0.23. The circular arrow indicates the direction of cylinder rotation. Note that tens of out-of-plane particles remained in the system, which were unremovable. (C) Temporal evolution of torque for different porosities ($\phi = 0.27\text{--}0.18$). Inset shows the definitions of torque drop amplitude ($\Delta\Gamma$) and duration (T). (D) Temporal evolution of tangential displacement of the cylinder surface, with color coding corresponding to panel (C).

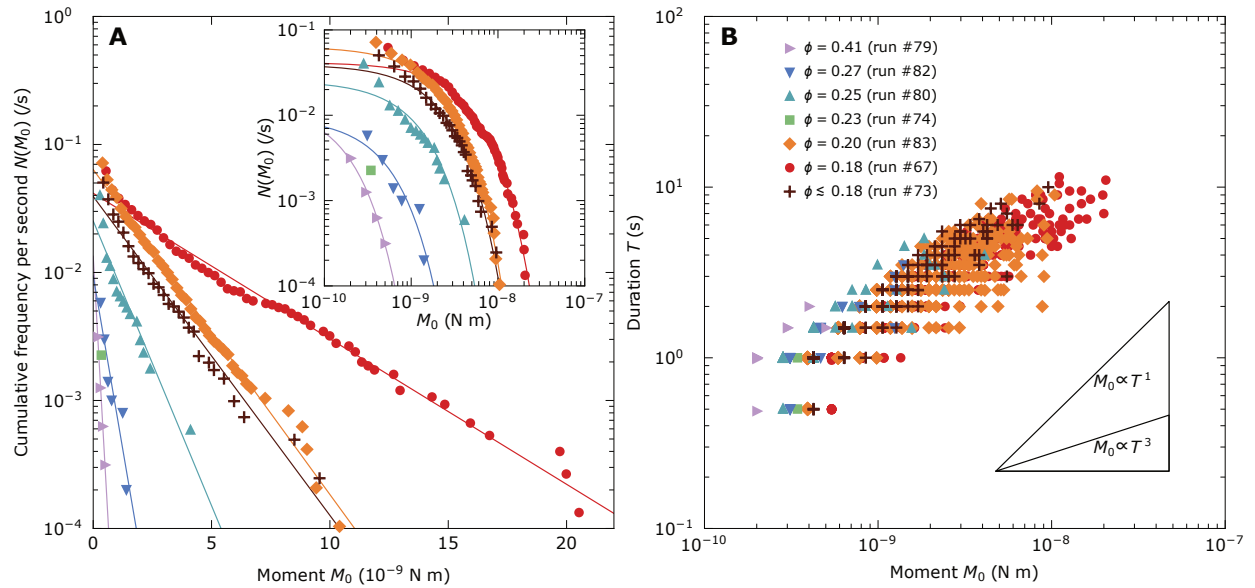
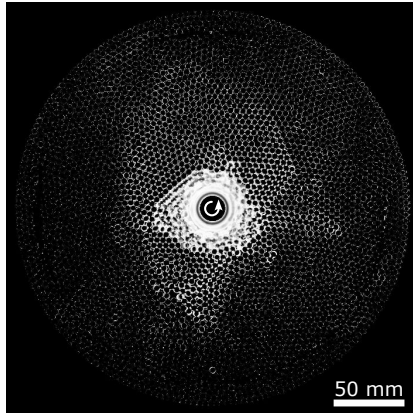


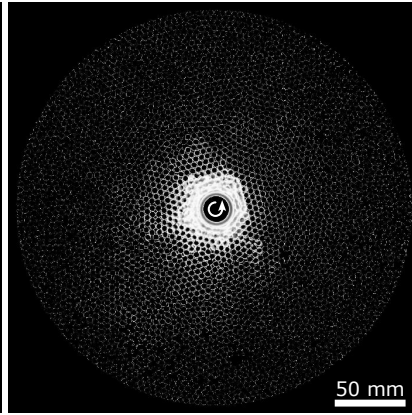
Figure 2: Statistical properties of the released moment. (A) Cumulative frequency distribution of the moment (per second). The linear trends in semi-logarithmic coordinates demonstrate exponential distributions, with fitting curves shown as solid lines. Inset shows the same data in a log-log plot. The colors and symbols correspond to those in (B). (B) Moment–duration relationship in logarithmic coordinates for porosities ranging from $\phi = 0.41$ to 0.18.

A Run #74, porosity $\phi = 0.23$



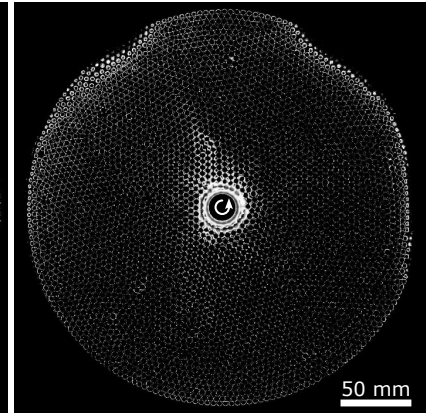
Sheared at $0.6^\circ/\text{s}$ for 1060 s
Shear band strain $\gamma \sim 5.5$

B Run #83, porosity $\phi = 0.20$



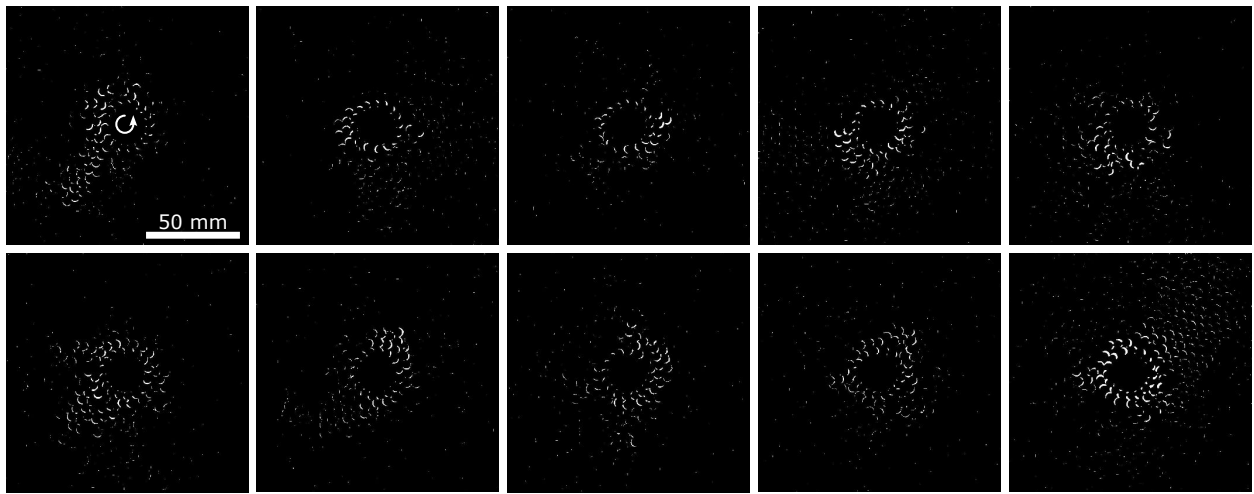
Sheared at $0.6^\circ/\text{s}$ for 1100 s
Shear band strain $\gamma \sim 7.0$

C Run #67, porosity $\phi = 0.18$



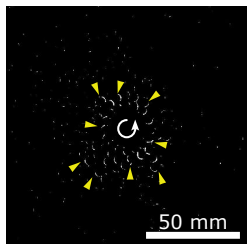
Sheared at $0.6^\circ/\text{s}$ for 1100 s
Shear band strain $\gamma \sim 12$

D Run #83, $\phi = 0.20$ (snapshot)

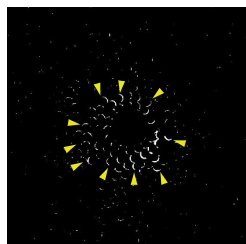


E Run #83, $\phi = 0.20$ (temporal evolution)

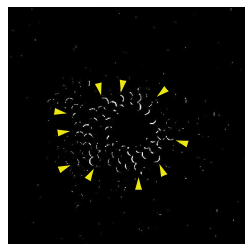
0.0–2.0 s



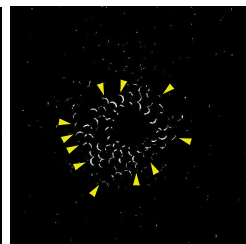
1.9–3.9 s



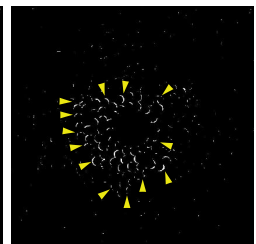
3.8–5.8 s



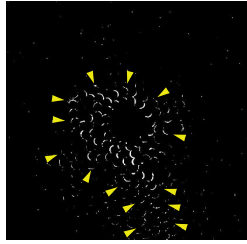
5.7–7.7 s



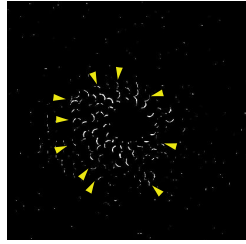
7.6–9.6 s



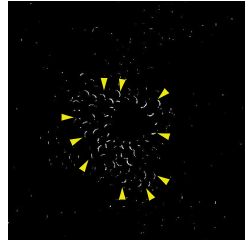
9.5–11.5 s



11.4–13.4 s



13.3–15.3 s



15.2–17.2 s

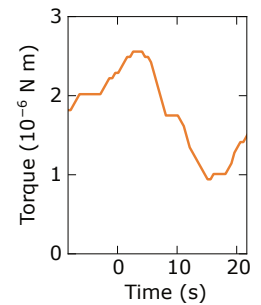
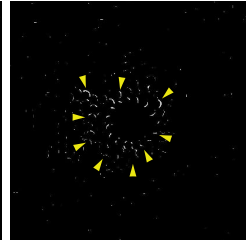


Figure 3: Shear band structures and particle motions responsible for torque drop events. (A, B, C) Shear band structures. Brightness corresponds to the standard deviations of binary videos recorded over approximately 1100 s at porosities $\phi = 0.23, 0.20,$ and $0.18,$ respectively. Shear strains $\gamma,$ estimated from shear band thickness $w,$ are approximately 5.5, 7.0, and 12, respectively. Note that (C) shows increased noise at edges owing to lighting conditions. (D) Typical patterns and area size of intermittent particle motions during different events. White areas represent particle-sweeping areas, obtained from binary image differences at a 2 s interval. A scale bar of 50 mm is common to all images. (E) Time series of particle motions corresponding to the consecutive torque drops. Image processing and the scale bar are the same as in (D). The time 0 s corresponds to a run time of 2228.3 s in run #83. Yellow arrows indicate the rupture front. Torque data corresponding to the images are shown in the last section. An animated version is available online in movie S1.

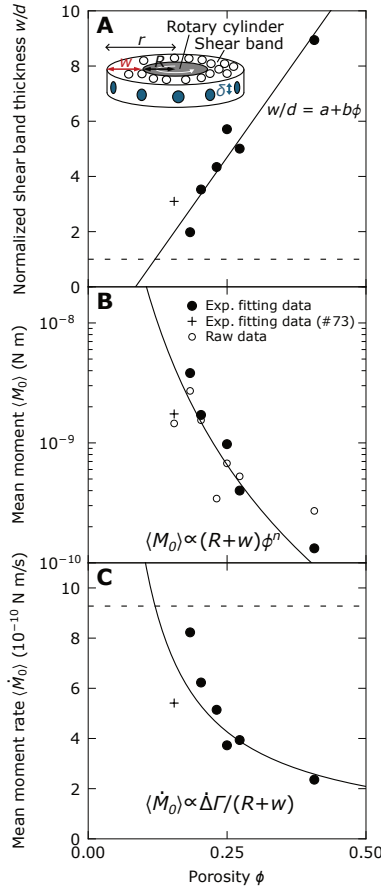


Figure 4: Effects of shear localization on the moment. (A) Shear band thickness normalized by the particle diameter as a function of porosity. Black circles represent experimental data. The solid line represents the linear fit with $a = -10.7$ and $b = 125$, excluding the cross symbol at the lowest porosity in run #73 ($0.15 \lesssim \phi \lesssim 0.18$), where many particles were not confined to the same monolayer. This exceptional datum is provisionally plotted at $\phi = 0.15$. The dashed line indicates the minimum thickness, $w/d = 1$. Inset indicates the schematic model of the shear band with the radial distance, $r = R + w$. (B) Mean moment as a function of porosity. The black and white circles represent the mean values from exponential fitting and raw data, respectively. The solid black line represents the fitting curve of all the solid circles (Equations 1 and equation S7), except for the cross symbol as in (A). (C) Mean moment rate as a function of porosity. The black circles represent the mean values and the solid black line indicates the reference curve of $\dot{M}_0 = M_0/T$ with constant slip velocity (Equation 1, 2). The dashed line indicates the maximum value at $w/d = 1$.

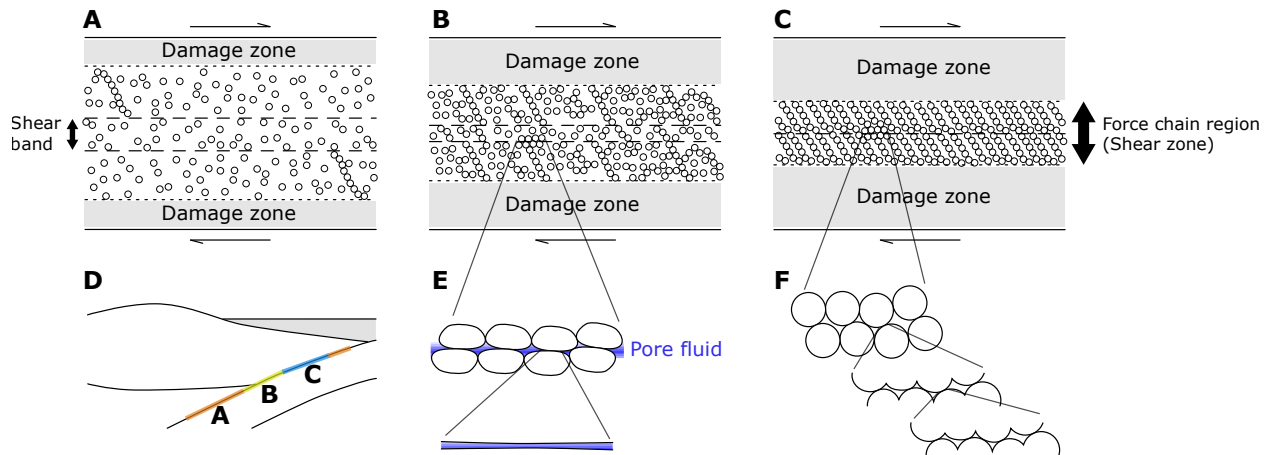


Figure 5: Schematic model of the granular fault core structures in slow and regular earthquakes. (A) Deeper region on the downdip transition zone (short-term slow earthquakes). A broad shear band is supported by long, weak force chains that are sparsely distributed across the shear zone. The white area represents pore fluid and/or ductile matrix (same for the following). (B) Shallower region on the downdip transition zone (long-term slow earthquakes). A localized shear band is supported by short, strong, and densely distributed force chains. (C) Seismogenic zone. Frictional, rigid force chains form networks throughout the shear zone, where growing ruptures lead to the generation of critical avalanches. (D) Cross-section of a subduction zone and plate interface. (E) Lubricated soft granular contact state in the fault core of slow earthquakes as (B). Pore fluid and/or ductile matrix concentrates within the shear band, and viscoelastically soft particles make the contact interface smoother and flatter, leading to slow earthquakes. (F) Frictional rigid granular contact state in the fault core of regular earthquakes as (C). Frictional particles with rough surfaces exhibit fractality, leading to self-similarity in faulting.

References and Notes

1. S. Ide, G. C. Beroza, D. R. Shelly, T. Uchide, A scaling law for slow earthquakes. *Nature* **447**, 76–79 (2007).
2. S. Ide, G. C. Beroza, Slow earthquake scaling reconsidered as a boundary between distinct modes of rupture propagation. *Proceedings of the National Academy of Sciences* **120**, e2222102120 (2023).
3. S. R. Chestler, K. C. Creager, Evidence for a scale-limited low-frequency earthquake source process. *Journal of Geophysical Research: Solid Earth* **122**, 3099–3114 (2017).
4. T. Watanabe, Y. Hiramatsu, K. Obara, Scaling relationship between the duration and the amplitude of non-volcanic deep low-frequency tremors. *Geophysical Research Letters* **34**, L07305 (2007).
5. D. R. Shelly, G. C. Beroza, S. Ide, S. Nakamura, Low-frequency earthquakes in Shikoku, Japan, and their relationship to episodic tremor and slip. *Nature* **442**, 188–191 (2006).
6. S. Y. Schwartz, J. M. Rokosky, Slow slip events and seismic tremor at circum-Pacific subduction zones. *Reviews of Geophysics* **45**, RG3004 (2007).
7. E. Araki, *et al.*, Recurring and triggered slow-slip events near the trench at the Nankai Trough subduction megathrust. *Science* **356**, 1157–1160 (2017).
8. T. Hirose, *et al.*, High fluid-pressure patches beneath the décollement: a potential source of slow earthquakes in the Nankai Trough off Cape Muroto. *Journal of Geophysical Research: Solid Earth* **126**, e2021JB021831 (2021).
9. T. Tonegawa, S. Takemura, S. Yabe, K. Yomogida, Fluid migration before and during slow earthquakes in the shallow Nankai subduction zone. *Journal of Geophysical Research: Solid Earth* **127**, e2021JB023583 (2022).
10. Q.-Y. Wang, W. B. Frank, R. E. Abercrombie, K. Obara, A. Kato, What makes low-frequency earthquakes low frequency. *Science Advances* **9**, eadh3688 (2023).

11. S. Ide, A brownian walk model for slow earthquakes. *Geophysical Research Letters* **35**, L17301 (2008).
12. K. Obara, A. Kato, Connecting slow earthquakes to huge earthquakes. *Science* **353**, 253–257 (2016).
13. Materials and methods are available as supplementary materials.
14. M. Ishimoto, K. Iida, Observations of earthquakes registered with the microseismograph constructed recently. *Bulletin of the Earthquake Research Institute* **17**, 443–478 (1939).
15. B. Gutenberg, C. F. Richter, Frequency of earthquakes in California. *Bulletin of the Seismological Society of America* **34**, 185–188 (1944).
16. Y. Hiramatsu, T. Watanabe, K. Obara, Deep low-frequency tremors as a proxy for slip monitoring at plate interface. *Geophysical Research Letters* **35**, L13304 (2008).
17. J. R. Sweet, “Unlocking the secrets of slow slip in Cascadia using low-frequency earthquakes,” thesis, University of Washington, Seattle (2014).
18. M. G. Bostock, A. M. Thomas, G. Savard, L. Chuang, A. M. Rubin, Magnitudes and moment-duration scaling of low-frequency earthquakes beneath southern Vancouver Island. *Journal of Geophysical Research: Solid Earth* **120**, 6329–6350 (2015).
19. M. Nakano, S. Yabe, Changes of event size distribution during episodes of shallow tectonic tremor, nankai trough. *Geophysical Research Letters* **48**, e2020GL092011 (2021).
20. H. Kanamori, D. L. Anderson, Theoretical basis of some empirical relations in seismology. *Bulletin of the Seismological Society of America* **65**, 1073–1095 (1975).
21. K. Aki, Scaling law of seismic spectrum. *Journal of Geophysical Research* **72**, 1217–1231 (1967).
22. B. Francois, F. Lacombe, H. J. Herrmann, Finite width of shear zones. *Physical Review E* **65**, 031311 (2002).

23. F. da Cruz, S. Emam, M. Prochnow, J.-N. Roux, F. Chevoir, Rheophysics of dense granular materials: Discrete simulation of plane shear flows. *Physical Review E* **72**, 021309 (2005).
24. C.-H. Liu, *et al.*, Force fluctuations in bead packs. *Science* **269**, 513–515 (1995).
25. A. Tordesillas, Force chain buckling, unjamming transitions and shear banding in dense granular assemblies. *Philosophical Magazine* **87**, 4987–5016 (2007).
26. D. M. Mueth, H. M. Jaeger, S. R. Nagel, Force distribution in a granular medium. *Physical Review E* **57**, 3164–3169 (1998).
27. L. E. Silbert, G. S. Grest, J. W. Landry, Statistics of the contact network in frictional and frictionless granular packings. *Physical Review E* **66**, 061303 (2002).
28. L. Zhang, Y. Wang, J. Zhang, Force-chain distributions in granular systems. *Physical Review E* **89**, 012203 (2014).
29. D. A. Geller, R. E. Ecke, K. A. Dahmen, S. Backhaus, Stick-slip behavior in a continuum-granular experiment. *Physical Review E* **92**, 060201 (2015).
30. E. Korkolis, A. R. Niemeijer, H. Paulssen, J. Trampert, A laboratory perspective on the Gutenberg-Richter and characteristic earthquake models. *Journal of Geophysical Research: Solid Earth* **126**, e2021JB021730 (2021).
31. A. Johansen, P. Dimon, C. Ellegaard, J. S. Larsen, H. H. Rugh, Dynamic phases in a spring-block system. *Physical Review E* **48**, 4779–4790 (1993).
32. M. A. Rubio, J. Galeano, Stick-slip dynamics in the relaxation of stresses in a continuous elastic medium. *Physical Review E* **50**, 1000–1004 (1994).
33. K. Aki, Generation and propagation of G waves from the Niigata earthquake of June 16, 1964. Part 2. Estimation of earthquake moment, released energy, and stress-strain drop from the G wave spectrum. *Bulletin of the Earthquake Research Institute* **44**, 73–88 (1966).
34. E. Aharonov, D. Sparks, Rigidity phase transition in granular packings. *Physical Review E* **60**, 6890–6896 (1999).

35. A. Abed Zadeh, J. Barés, J. E. S. Socolar, R. P. Behringer, Seismicity in sheared granular matter. *Physical Review E* **99**, 052902 (2019).
36. C. Liu, E. E. Ferrero, F. Puosi, J.-L. Barrat, K. Martens, Driving rate dependence of avalanche statistics and shapes at the yielding transition. *Physical Review Letters* **116**, 065501 (2016).
37. P. D. Ispánovity, *et al.*, Avalanches in 2D dislocation systems: Plastic yielding is not depinning. *Physical Review Letters* **112**, 235501 (2014).
38. Z. Budrikis, S. Zapperi, Avalanche localization and crossover scaling in amorphous plasticity. *Physical Review E* **88**, 062403 (2013).
39. F. Dalton, D. Corcoran, Self-organized criticality in a sheared granular stick-slip system. *Physical Review E* **63**, 061312 (2001).
40. H. M. Savage, C. D. Rowe, Localization and delocalization during seismic slip. *Geophysical Research Letters* **51**, e2024GL110058 (2024).
41. A. M. Thomas, R. M. Nadeau, R. Bürgmann, Tremor-tide correlations and near-lithostatic pore pressure on the deep San Andreas fault. *Nature* **462**, 1048–1051 (2009).
42. D. M. Saffer, L. M. Wallace, The frictional, hydrologic, metamorphic and thermal habitat of shallow slow earthquakes. *Nature Geoscience* **8**, 594–600 (2015).
43. R. Ando, K. Ujiie, N. Nishiyama, Y. Mori, Depth-dependent slow earthquakes controlled by temperature dependence of brittle-ductile transitional rheology. *Geophysical Research Letters* **50**, e2022GL101388 (2023).
44. J. D. Kirkpatrick, Å. Fagereng, D. R. Shelly, Geological constraints on the mechanisms of slow earthquakes. *Nature Reviews Earth & Environment* **2**, 285–301 (2021).
45. W. M. Behr, R. Bürgmann, What’s down there? The structures, materials and environment of deep-seated slow slip and tremor. *Philosophical Transactions of the Royal Society A: Mathematical, Physical and Engineering Sciences* **379**, 20200218 (2021).
46. J. H. Dieterich, Modeling of rock friction: 1. Experimental results and constitutive equations. *Journal of Geophysical Research: Solid Earth* **84**, 2161–2168 (1979).

47. A. Ruina, Slip instability and state variable friction laws. *Journal of Geophysical Research: Solid Earth* **88**, 10359–10370 (1983).
48. C. Marone, Laboratory-derived friction laws and their application to seismic faulting. *Annual Review of Earth and Planetary Sciences* **26**, 643–696 (1998).
49. H. Gao, D. A. Schmidt, R. J. Weldon, Scaling relationships of source parameters for slow slip events. *Bulletin of the Seismological Society of America* **102**, 352–360 (2012).
50. K. Obara, Characteristic activities of slow earthquakes in Japan. *Proceedings of the Japan Academy, Series B* **96**, 297–315 (2020).
51. R. H. Sibson, Tensile overpressure compartments on low-angle thrust faults. *Earth, Planets and Space* **69**, 113 (2017).
52. C. G. Sammis, M. G. Bostock, A granular jamming model for low-frequency earthquakes. *Journal of Geophysical Research: Solid Earth* **126**, e2021JB021963 (2021).
53. Z. Ma, *et al.*, Slow rupture in a fluid-rich fault zone initiated the 2024 M_w 7.5 Noto earthquake. *Science* **385**, 866–871 (2024).
54. Y. Sasaki, H. Katsuragi, Experimental data for “Origin of slow earthquake statistics in low-friction soft granular shear”, version 1, Zenodo (2025), <https://doi.org/10.5281/zenodo.14736870>.
55. J. Schindelin, *et al.*, Fiji: an open-source platform for biological-image analysis. *Nature Methods* **9**, 676–682 (2012).
56. J. P. Gong, Friction and lubrication of hydrogels—its richness and complexity. *Soft Matter* **2**, 544–552 (2006).
57. I. Ishibashi, C. Perry, T. K. Agarwal, Experimental determinations of contact friction for spherical glass particles. *Soils and Foundations* **34**, 79–84 (1994).
58. F. X. Passelègue, *et al.*, Initial effective stress controls the nature of earthquakes. *Nature Communications* **11**, 5132 (2020).

59. M. R. Gregory, K. A. Johnston, A nontoxic substitute for hazardous heavy liquids — aqueous sodium polytungstate ($3\text{Na}_2\text{WO}_4 \cdot 9\text{WO}_3 \cdot \text{H}_2\text{O}$) solution (Note). *New Zealand Journal of Geology and Geophysics* **30**, 317–320 (1987).
60. G. L. Skipp, I. K. Brownfield, Improved density gradient separation techniques using sodium polytungstate and a comparison to the use of other heavy liquids. *Open-File Report (U.S. Geological Survey)* **92–386**, 1–16 (1993).
61. N. Higashi, I. Sumita, Experiments on granular rheology: Effects of particle size and fluid viscosity. *Journal of Geophysical Research: Solid Earth* **114**, 2008JB005999 (2009).
62. P. M. Shearer, “9. Earthquakes and source theory”, in *Introduction to Seismology* (Cambridge University Press, ed. 2, 2009), pp. 241–299.
63. L. Knopoff, Energy release in earthquakes. *Geophysical Journal International* **1**, 44–52 (1958).
64. J. D. Eshelby, The determination of the elastic field of an ellipsoidal inclusion, and related problems. *Proceedings of the Royal Society of London. Series A. Mathematical and Physical Sciences* **241**, 376–396 (1957).

Acknowledgments

We acknowledge with gratitude the thoughtful and specialized comments of O. Kuwano and F. Nakai. We are sincerely thankful to R. Ando for his advice from the perspective of seismology to form this research’s direction. We would like to thank Editage (www.editage.jp) for English language editing.

Funding: This work was supported in part by the Sasakawa Scientific Research Grant from the Japan Science Society 2024-6006 funded to Y. S., and by JSPS KAKENHI Grant Numbers JP23H04134, JP24H00196 funded to H. K.

Author contributions: Y.S. and H.K. conceptualized this experimental study, administered and managed the project, and reviewed and edited the drafts. Y.S. performed investigations, designed the

experimental apparatus, established the measurement methodology, curated and formally analyzed data using software coding, visualized data into figures, and wrote an original draft. H.K. supervised this project, provided and installed the experimental equipment, and validated the data and results.

Competing interests: There are no competing interests to declare.

Data and materials availability: All data underlying all figures are available as CSV file format (CC-BY 4.0) on Zenodo (54) at <https://doi.org/10.5281/zenodo.14736870>. Analyzing the recorded images was performed with FIJI/IMAGEJ Version 2.14.0/1.54f software (55) in <https://imagej.net/software/fiji/> as open source (GNU GPL).

Supplementary materials

Materials and Methods

Supplementary Text

Figs. S1 to S8

Tables S1

References (56-64)

Movie S1

Supplementary Materials for Origin of slow earthquake statistics in low-friction soft granular shear

Yuto Sasaki*, Hiroaki Katsuragi

*Corresponding author. Email: sasaki.geoscience@gmail.com

This PDF file includes:

Materials and Methods

Supplementary Text

Figures S1 to S8

Table S1

Captions for Movie S1

Other Supplementary Materials for this manuscript:

Movie S1

Materials and Methods

We conducted rotary shear experiments on a floating granular monolayer, showing stick-slip behaviors. We measured torque and recorded the particle arrangement in situ, varying the porosity of the layer from 0.18 to 0.41 and the granular material, with the other conditions held constant. The temporal evolution of mechanical torque and visual data are quantified, and the statistical relationship between them was investigated.

Experimental Setup

The experimental setup is shown in Fig. 1A. We sheared a layer of particles floating on a heavy liquid surface in a cylindrical container at room temperature and atmospheric pressure by inserting a rotating cylinder into the center of the layer. The floating particles comprise an approximately one-particle-thick monolayer, enabling the tracking of all particles with a camera. This floating granular system removes the effects of basal and interparticle frictions.

We used opaque spherical polymer hydrogel particles (CHARM, Bio Beads 56975, PEG) and spherical glass beads (Bright Beads, Y-4, soda-lime glass) as the fault gouge analogue. Hydrogel spheres with lower friction [coefficient of $< 10^{-1}$ (56)] and lower modulus [\sim kPa], and glass beads with friction [coefficient of $\gtrsim 0.2$ (57)] and higher modulus [\sim GPa] were floated in quasi-two-dimensional geometry. This lubricated granular layer is appropriate to simulate low effective stress owing to high pore pressure, widely suggested as a cause of regular and slow earthquakes (58). To align particle centroids within the same plane on the liquid, we used particles with a diameter of $d = 4.4$ mm with a standard deviation of 0.1 mm for hydrogel, and $d = 4.1$ mm for glass beads. We measured the diameter using approximately 2000 particles at Run #74 (table S1). We immersed the particles in the heavy liquid solution for preparation for more than one week, as the hydrogel particles change volume owing to osmotic pressure depending on the concentration of the solution. The osmotic effect makes the particles shrink by 2–3% in diameter, 5 days after starting the permeation of the water-immersed particles.

To float the particles, we used a transparent solution of sodium polytungstate ($\text{Na}_6(\text{H}_2\text{W}_{12}\text{O}_6)$, TC-Tungsten Compounds GmbH, purity of $> 99\%$) with a density of 2.8 g/cm^3 and viscosity of approximately $2 \times 10^{-2} \text{ Pa s}$, both of which depend on the concentration (59, 60). The density

makes the particles remain suspended just below the liquid surface level, as schematically shown in Fig. 1A. To prepare the solution, sodium polytungstate powder is dissolved in deionized water by stirring. We measured the density and concentration of the solution by Archimedes' method. In all experiments, the depth of this liquid solution was approximately 10 mm, greater than twice the particle diameter. This enables the particles to move under an adjacent particle without any stiffening by the resistance from the base of the container.

This Couette system is composed of a container with a diameter of 300 mm and a central rotating cylinder with a diameter of $R = 9.42$ mm. The same 16 particles were glued in a single row around the side surface of the cylinder. The ratio of the channel width to the particle diameter is 34 (Fig. 1B). To investigate the effect of system size, we also performed the same experiments using another container with a 100 mm diameter and a cylinder of $R = 9.36$ mm, onto which the same 17 particles were glued.

To rotate the cylinder and measure the torque, we used a B-type viscometer (BROOKFIELD, LVDV-II+Pro, maximum torque of 6.73×10^{-5} N m and rotation speed of 6×10^{-2} – 1.2×10^3 °/s). The motor of the viscometer was set to rotate unidirectionally at a constant rate ω , which was not directly measured. The cylinder and the motor were connected through a torsion spring with a rotational stiffness of $K = 9.75 \times 10^{-7}$ N m/°. The rotation rate of 0.6°/s is considered quasi-static and sufficiently slow to neglect the fluid inertial effect with a particle Reynolds number of $Re_p \simeq 0.1$, assuming viscosity, velocity, fluid density, and particle diameter of 2×10^{-2} Pa s, 0.1 mm/s, 2.8 g/cm³, 4 mm, respectively.

To record and track the motion of all particles in situ, the cylindrical container has a transparent base plane. We used a USB vision camera (OMRON SENTECH, STC-MCCM401U3V, effective pixels of 2048×2048 , maximum frame rate of 89 fps) with a machine vision lens (RICOH OPTOWL, FL-BC1220-9M). For technical convenience, we used a mirror inclined at 45° and set the camera horizontally. To ensure the alignment of the optical axis, we adjusted the top of the viscometer, container base, and top of the camera to horizontal direction, by visually checking a level. We also verified that the center of the container base was aligned with the center of the camera's field of view on the screen, with the accuracy of a few pixels. When recording, we placed two panel light sources on both sides of the apparatus to enhance the contrast (Fig. 1B).

In the experimental procedure, we first filled the container with the liquid, added particles,

manually stirred the mixture thoroughly, and subsequently inserted the cylinder of the viscometer. We adjusted the height position of the particles glued to the cylinder to ensure that they coincide with the floating level of the particle layer. We subsequently removed the particles trapped at the bottom of the cylinder. Finally, we started shearing the granular layer by the rotating cylinder, logging torque, and simultaneously recording images.

Experimental Conditions

The shear experiments were performed in 18 runs, as summarized in table S1. We investigated the dependence of mechanical behaviors on the particle number (approximately 4000 at maximum and porosity $\phi = 0.18$ at minimum), particle type ($d = 4.4$ mm hydrogel, 4.1 mm glass beads, and 2 mm glass beads), and rotation angular velocity ($\omega = 0.06\text{--}60^\circ/\text{s}$). The range of porosity was chosen to ensure that the granular layer can maintain single-layer thickness and also exhibit any detectable torque resistance. We conducted experiments for hundreds to tens-of-thousand seconds, depending on the runs. The rotation rate of the viscometer motor, liquid concentration, system size, and other conditions were kept constant.

We estimated the porosity of the granular layer using the mean particle diameter d and number counted using the recorded image (Fig. 1B). This value is used as porosity in this study. We also evaluated whether the estimated porosity is consistent with the visually measured value. In particular, in the case of run #73 using approximately 4000 particles, many particles are out of the monolayer plane. Its porosity is estimated to be between 0.15 (assuming all particles are confined within the monolayer) and 0.18 (of run #67 with fewer particles). We provisionally plotted its data in Fig. 4 and fig. S2 at $\phi = 0.15$. Confining all particles within a single layer is difficult at lower porosity ($\phi < 0.3$), leading to some particles being located out of the plane. We intentionally arranged the particles in a polycrystalline structure in runs #67 and #70 to investigate the effect of crystallization. In run #67, lightning and optical alignment conditions caused a low signal-to-noise ratio in the image, as shown in Fig. 3C.

Measurements

We measured the torque and recorded the images immediately after starting the rotational shear. The torque was measured at a sampling rate of approximately 2 Hz. With the viscometer, the nominal

minimum value of torque measurement was 6.73×10^{-7} N m, namely, 1% of the maximum. We recorded the visual images with an exposure time of 0.1 s at a sampling rate of 10 fps. In our experimental setup, a unit pixel corresponds to approximately 0.16 mm at the center of the images. For all images, we did not apply any correction for optical refraction, distortion, and misalignment, which does not significantly affect the results in this study qualitatively. The distortion between the center and edge of the 300 mm container was 2% at maximum, and the shear bands we analyzed were localized to the central part of the images. In each run, torque measurement and image acquisition were initiated manually at the same time. The accuracy of temporal synchronization between mechanical data and the visual image was approximately 0.1 s, evaluated by the recording test at 10 fps. Examples of the recorded dataset are shown in fig. S1.

Analysis

We defined the run time by excluding data at the beginning and final 100 s of each run, and quantified both the mechanical and visual data over the remaining run duration. These exceptional data possibly include unsteady transient flow and noise owing to vibrations and perturbations by the operation of the viscometer.

First, using the mechanical data, we quantitatively characterized the temporal fluctuation of torque $\Gamma(t)$. Torque drop duration T and drop amplitude $\Delta\Gamma = -(\Gamma(t_1 + T) - \Gamma(t_1)) > 0$ with start time t_1 are characterized for each event. The values $\Delta\Gamma = \Delta\Gamma^i$, $T = T^i$, $t_1 = t_1^i$ for the i -th event are defined such that $\dot{\Delta\Gamma}(t) < 0$ is always satisfied in the range of $t_1^i \leq t < t_1^i + T^i$ and $\dot{\Delta\Gamma}(t) \geq 0$ at $t = t_1^i - dt$, $t_1^i + T^i$ with a sampling interval of $dt \approx 0.5$ s (inset of Fig. 1C). Here, the letter i in the upper-right of the variables is the index corresponding to the i -th event.

Although we did not set any threshold value for the definition of the magnitude of torque and its drop amplitude, the events with $\Delta\Gamma \leq 6.73 \times 10^{-8}$ N m (the practically measurable minimum value) were excluded from the analysis. We analyzed approximately 10–6500 torque drop events, depending on the run duration, as presented in table S1. Event counts are normalized to the duration of each experimental run.

The cumulative frequency of torque drop amplitude per second was calculated as follows (note

that torque drop amplitude is treated as moment for the moment statistics):

$$N(\Delta\Gamma) = \int_{\Delta\Gamma}^{\Delta\Gamma_{\max}} n(\Delta\Gamma') d\Delta\Gamma', \quad (\text{S1})$$

where $\Delta\Gamma_{\max}$ is the maximum value of torque drop amplitude for each run, and $n(\Delta\Gamma') d\Delta\Gamma'$ is an event count normalized by the entire run duration (/s), with torque drop amplitude in the range between $\Delta\Gamma'$ and $\Delta\Gamma' + d\Delta\Gamma'$. As the cumulative frequency follows a nearly exponential distribution (fig. S3A for torque drop, Fig. 2A for moment), we fit the following function to data as,

$$N(\Delta\Gamma) = N(0) \exp\left(-\frac{\Delta\Gamma}{G}\right), \quad (\text{S2})$$

where $N(0)$ and G are the fitting parameters. When an ideal exponential distribution is satisfied, $G = \langle \Delta\Gamma \rangle$, where $\langle \rangle$ denotes the mean value. We obtained the mean torque drop amplitude as the value of fitting parameter G .

From the torque data, we also estimated the rotating cylinder displacement $u(t)$ along the side surface of the cylinder. To obtain the displacement, we applied the correction for the apparatus stiffness to the torque data as shown in equation 2 in (6I). Using the torsional stiffness of the viscometer $K = 9.753 \times 10^{-7}$ (N m/°), constant angular velocity ω (°/s) of the motor, and radius of the rotating cylinder R , displacement on the side surface of the cylinder can be calculated as,

$$u(t) = \frac{K\omega t - \Gamma(t)}{\frac{360K}{2\pi R}}. \quad (\text{S3})$$

$u(t)$ can be considered the displacement imposed on the granular layer itself, deforming it elastically and plastically.

Second, using the sequential recorded images of particle arrangements, we applied two types of image processing using FIJI/IMAGEJ software (55): time-lapse and differential images (Fig. 3). To process these images, we first obtained binary images generated according to the contrast difference between the particle areas and background. For analysis, we used the images recorded during 1000 s and more than 1000 s after the beginning of the experiments, which capture the steady arrangement of particles. As an exception, we used images captured immediately after the beginning of run #67 and 600 s after the beginning of runs #74 and #80 to obtain adequate amounts of recorded images. These exceptional data possibly include unsteady transient flow and noise owing to vibrations and perturbations by the operation of the viscometer.

For the time-lapse images (Fig. 3A–C), we mapped the standard deviation for each pixel over the entire duration of 1000 s. For the differential images, we also calculated the absolute difference in brightness between binary snapshots holding a 2-second gap every 0.1 s (10 fps). We chose the relatively long time gap (2 s) to capture adequate differences between frames as several pixels in each differential image.

Using original binary images, we measured the number of particles (Fig. 1B). Using the time-lapse images, we characterized the spatial distribution of shear bands and measured their thickness based on the radial distribution of brightness value (Figs. 3A–C, 4A). Using the differential images, we quantitatively analyzed the motion area where particles have swept (Fig. 3D, E, fig. S1). In addition, to investigate the apparent slip plane size for each event, we also estimated the number of drifting particles p at each time. To calculate p , we used the ratio of the differential area over the entire region, a , to that per particle over the region with a radius of $r = R + d$ with the fixed particles on the cylinder, a_c , resulting in $p = a/a_c$. This value p can be used as an estimate of the equivalent slip plane area S . We statistically analyzed the value p averaged over each duration T for each event (fig. S4).

Supplementary Text

Estimation of the moment from torque drop amplitude and shear band thickness

Moment M_0 of slip associated with stress drop $\Delta\sigma$ is represented as,

$$M_0 = \mu SD = \frac{LS}{C} \Delta\sigma, \quad (\text{S4})$$

where μ is the shear modulus, S is the slip area, D is the slip displacement, L is the slip patch width, $\Delta\sigma$ is the stress drop, and C is the geometrical constant (33, 62). The stress drop is represented as (62–64),

$$\Delta\sigma = C\mu \frac{D}{L}. \quad (\text{S5})$$

Considering the cylindrical shape of a shear band with stress applied to the side wall, as shown in the inset of Fig. 4A, the shear stress drop $\Delta\sigma(r)$ with radial distance r from the center of the rotation axis is related to the torque drop amplitude $\Delta\Gamma(r)$ as,

$$\Delta\sigma(r) = \frac{\Delta\Gamma(r)}{2\pi r^2 \delta}, \quad (\text{S6})$$

with the diameter δ of the interparticle contact area, and $L = \delta$, $S = 2\pi r\delta$ under the assumption that the moment arm is mechanically homogeneous. Considering the conservation of angular momentum of the shear band under steady state, the measured torque drop amplitude on the cylinder $\Delta\Gamma$ can be considered in equilibrium with the torque drop amplitude on the outer side wall of the shear band $\Delta\Gamma(r = R + w)$, with radius of the rotating cylinder R and shear band thickness w . Using equations S4, S5, and S6, we can obtain Equation 1. We assume the following values: $C = 7\pi/16$ for the circular crack at each contact patch (64), and constant $\delta = 0.1$ mm, which is expected to increase with decreasing porosity in practice.

Model fitting of the moment and moment rate as a function of porosity

Moment $M_0(\Delta\Gamma)$ in Equation 1 is represented using torque drop amplitude $\Delta\Gamma$ as,

$$\Delta\Gamma = (R + w)[2\pi(R + w)\delta]\Delta\sigma, \quad (\text{S7})$$

when considering the cylindrical shear band. The mean moment data $\langle M_0 \rangle(\phi)$, obtained from the exponential fitting of the cumulative frequency distribution (Fig. 2A), are adequately explained when we use $w(\phi)$ relationship and fit $\Delta\sigma = A\phi^n$ to the mean torque drop amplitude data $\langle \Delta\Gamma \rangle(\phi)$, except for run #73 (solid curve in Fig. S2B). The fitting results are $A = 4.7 \times 10^{-13}$ Pa and $n = -5.0$, shown as a solid curve in Fig. 4B. We also fit another function of $\Delta\sigma = B(1 - \phi)^m$ with $B = 1.78 \times 10^{-8}$ Pa and $m = 12$ (dashed curve in Fig. S2B).

Moment rate $\dot{M}_0 = M_0/T$ is represented as,

$$\dot{M}_0 = \frac{M_0}{\bar{D}/\bar{V}}, \quad (\text{S8})$$

where \bar{D} is the tangential slip displacement of the cylinder and $\bar{V} = \bar{D}/T$ is the tangential slip velocity of the cylinder averaged over each event duration. As \bar{D} is calculated from displacement $u(\Gamma)$ in Equation S3, we obtain Equation 2, where $\Delta\Gamma/T$ is trivially expressed with a single variable \bar{V} . The analytical curve of equation S8 using Equation 1, 2 is shown in Fig. 4C as a solid line, with a constant mean value of $\bar{V} = 0.128$ mm/s (figs. S2D, S8) and $w(\phi)$ relationship (Fig. 4A).

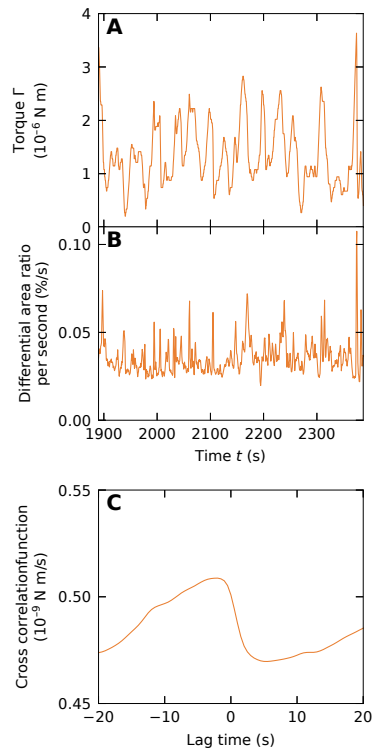


Figure S1: Correlation between the torque and particle motion. The data were obtained in run #83 ($\phi = 0.20$). **(A)** Torque data. **(B)** Differential area ratio normalized to the whole area per second. **(C)** Cross-correlation function between the torque and differential area ratio per second without normalization.

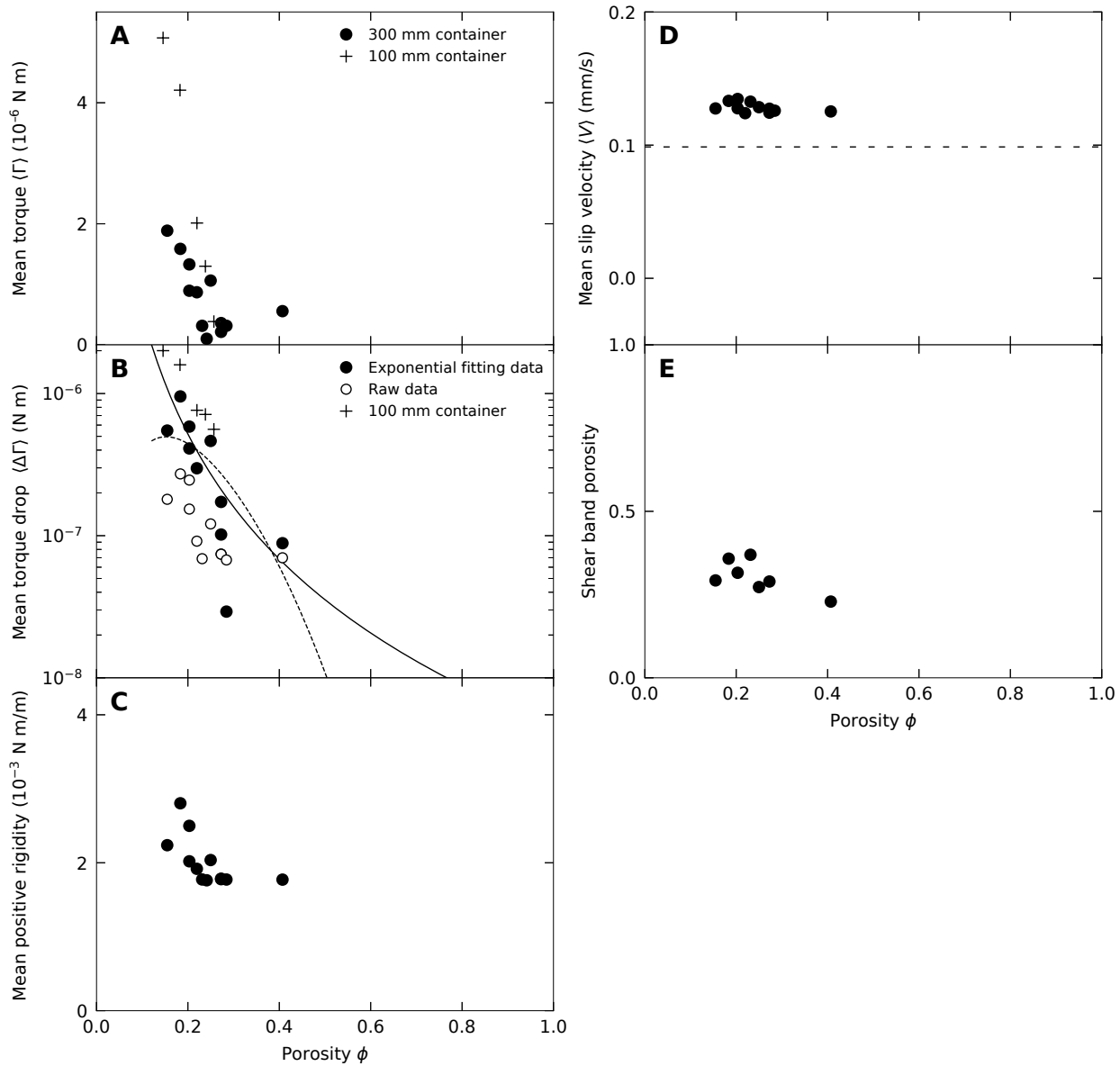


Figure S2: Porosity dependence of measured variables. (A) Mean torque. The black circles correspond to the mean data using the 300 mm container and the cross symbols are the data using the 100 mm container for comparison. (B) Mean torque drop amplitude. The solid circles correspond to the means obtained from the exponential fitting and the open circles are the means calculated from raw data in fig. S3. The cross symbols correspond to the means obtained from the exponential fitting using the 100 mm container. The solid and dashed fitting curves are represented by equation S7 using $\Delta\sigma = A\phi^n$ ($A = 4.7 \times 10^{-13}$ Pa, $n = -5.0$) and $\Delta\sigma = B(1 - \phi)^m$ ($B = 1.78 \times 10^{-8}$ Pa, $m = 12$), respectively. (C) Mean positive rigidity calculated as the ratio of torque increment to displacement increment between adjacent time steps. (D) Mean slip velocity on the surface of rotating cylinder. The dashed line indicates the constant motor velocity without any torque resistance. (E) Measured porosity within the shear band with a thickness w .

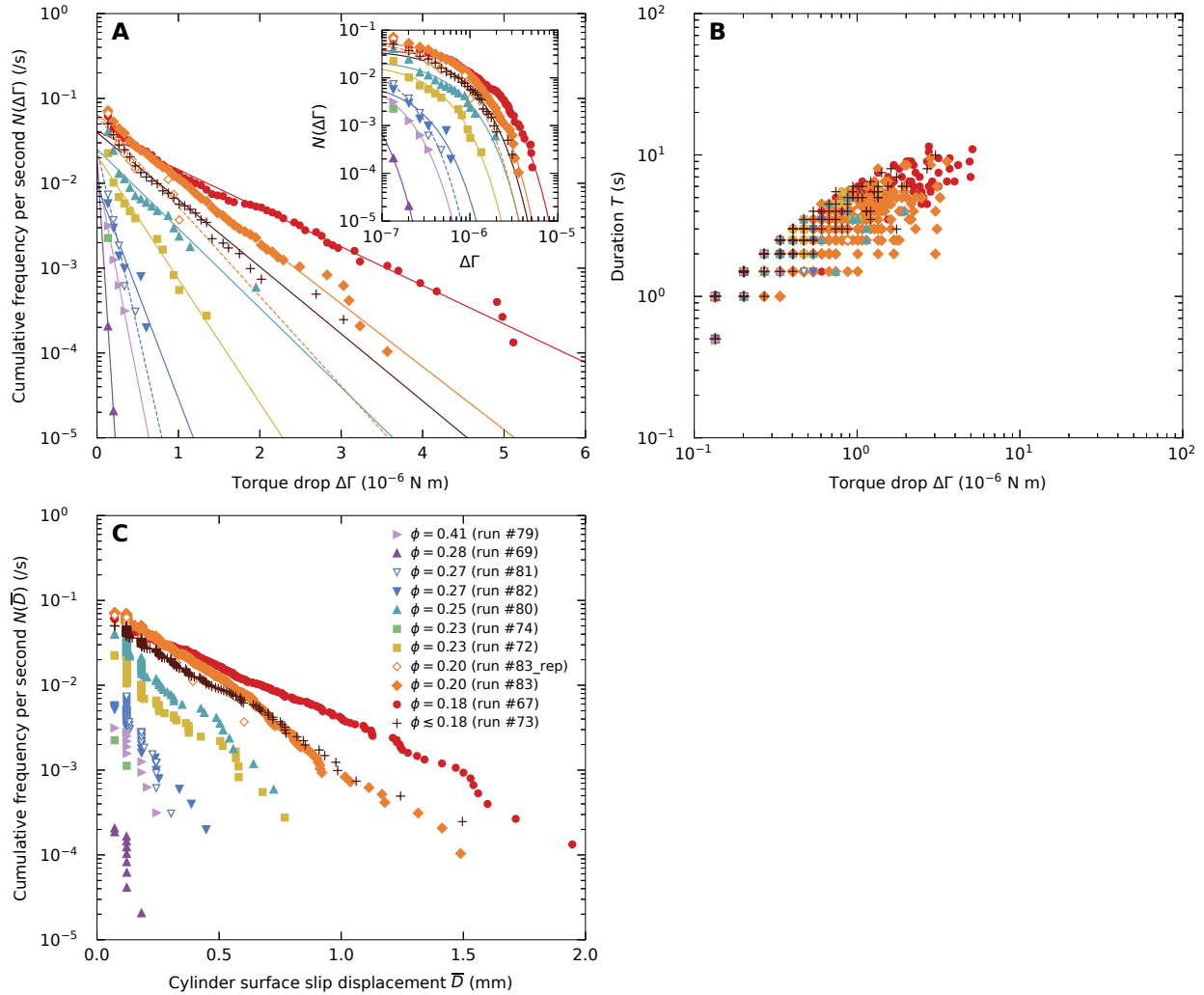


Figure S3: Statistical characteristics of torque drop events in the system with diameter of 300 mm. The symbols and colors are common in all subplots. (A) Cumulative distribution of the torque drop amplitude $\Delta\Gamma$. Inset shows the same data in a log-log plot. (B) Relationship between the torque drop amplitude and duration. (C) Cumulative frequency distribution of the tangential slip displacement \bar{D} on the surface of cylinder.

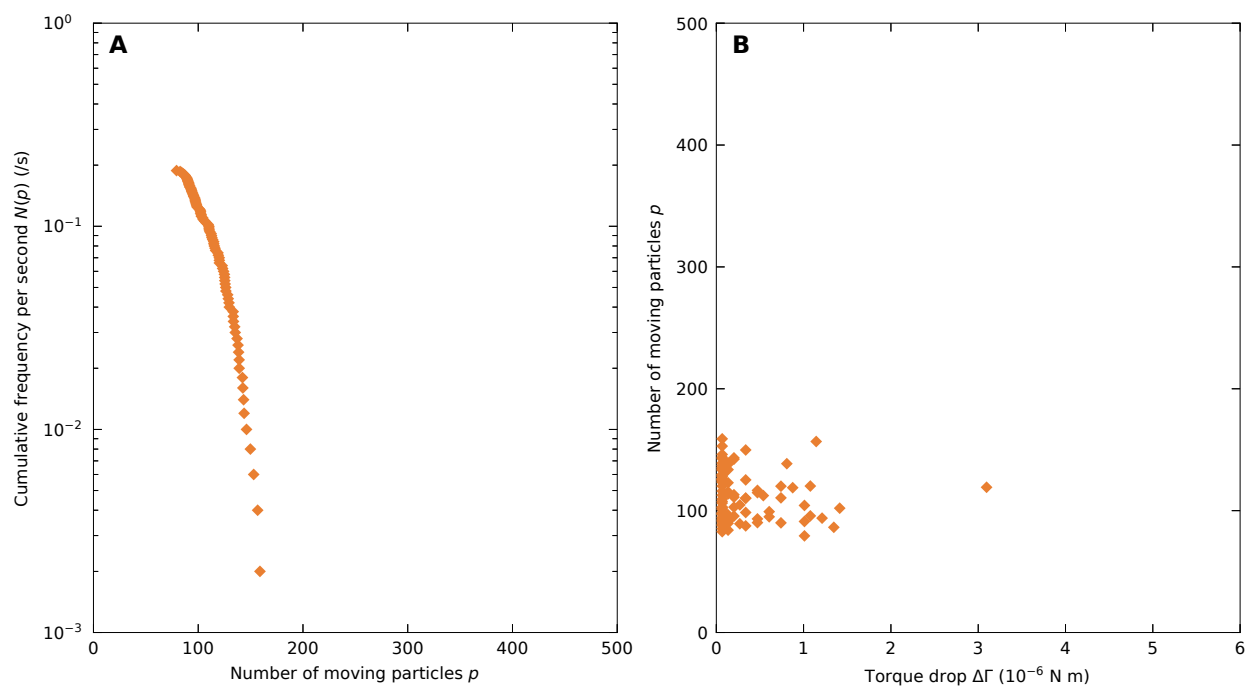


Figure S4: Distribution of the particle number related to the slip events. The data were obtained from the run time of $t = 1890$ – 2387 s in run #83 ($\phi = 0.20$). **(A)** Cumulative frequency distribution of the number of moving particles p . **(B)** Number of moving particles depending on the torque drop amplitude.

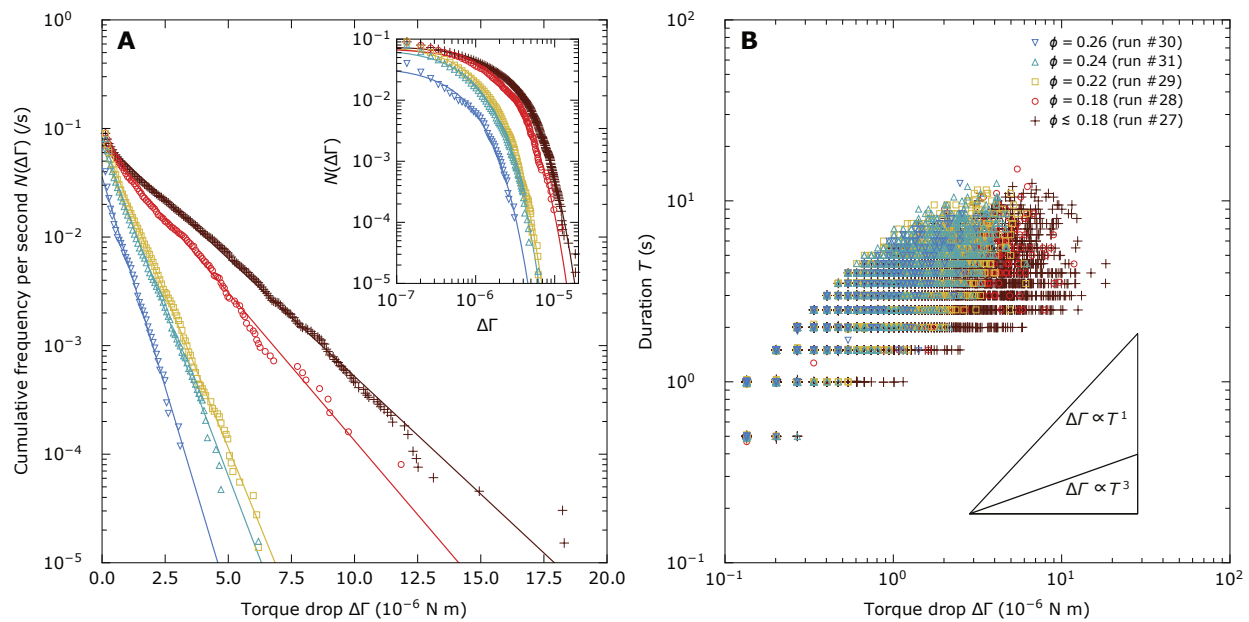


Figure S5: Statistical characteristics of torque drop events in the system with diameter of 100 mm. The symbols and colors are common in all subplots. **(A)** Cumulative distribution of the torque drop amplitude $\Delta\Gamma$. Inset shows the same data in a log-log plot. **(B)** Relationship between the torque drop amplitude and duration.

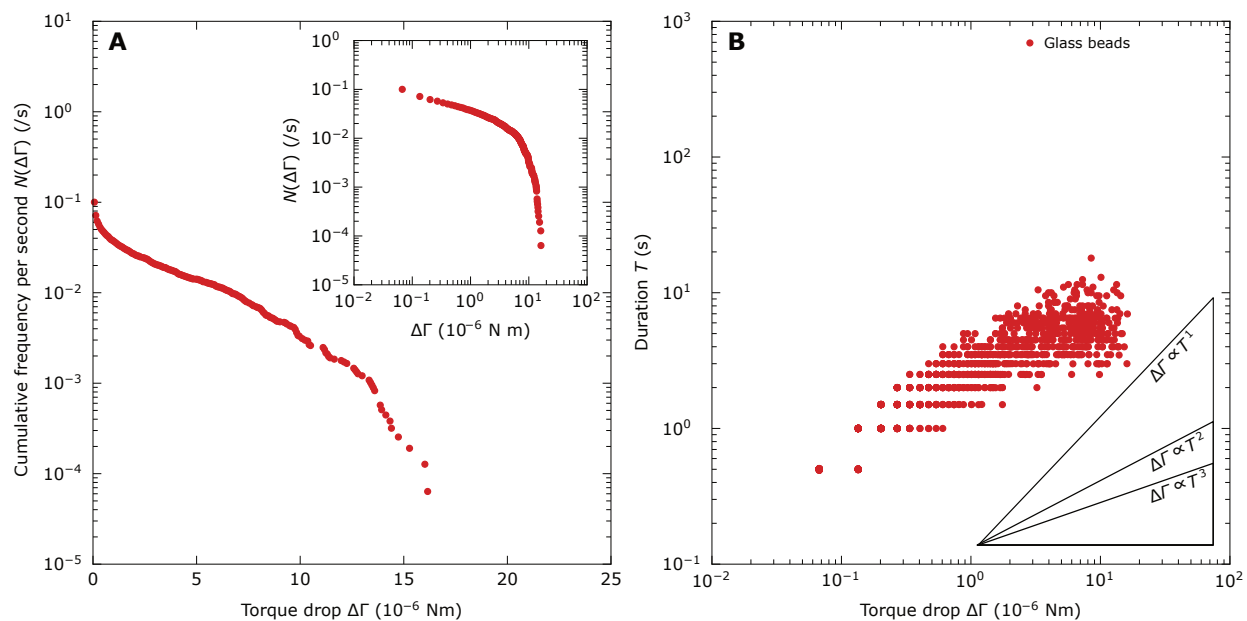


Figure S6: Statistical characteristics of torque drop events in the system with diameter of 300 mm using glass beads. The data were obtained in run #87 using 4760 glass beads with a diameter of 4.1 mm. **(A)** Cumulative frequency distribution of the torque drop amplitude $\Delta\Gamma$. Inset shows the same data in a log-log plot. **(B)** Relationship between the torque drop amplitude and duration.

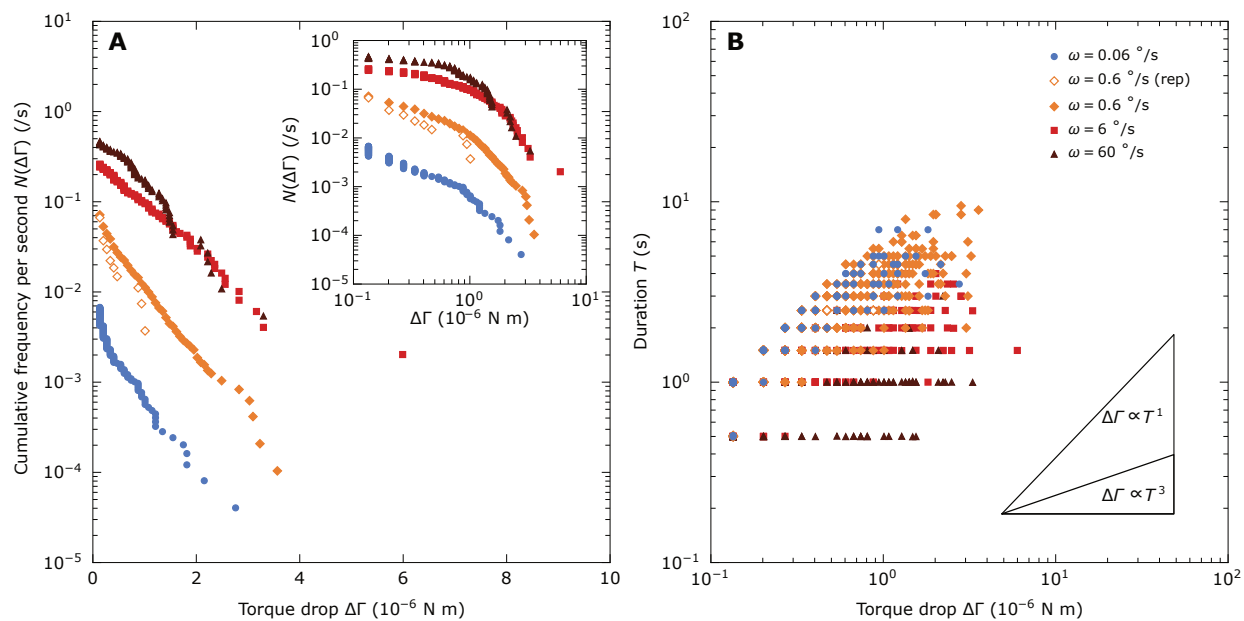


Figure S7: Statistical characteristics of torque drop events at various rotation rates. All data are obtained in run #83 ($\phi = 0.20$). **(A)** Cumulative frequency distribution of the torque drop amplitude $\Delta\Gamma$. Inset shows the same data in a log-log plot. The symbols and colors are the same as **(B)**. **(B)** Relationship between the torque drop amplitude and duration. The symbols and colors correspond to the rotation rates of $\omega = 0.06$ – 60 °/s. The open symbols correspond to the replication test.

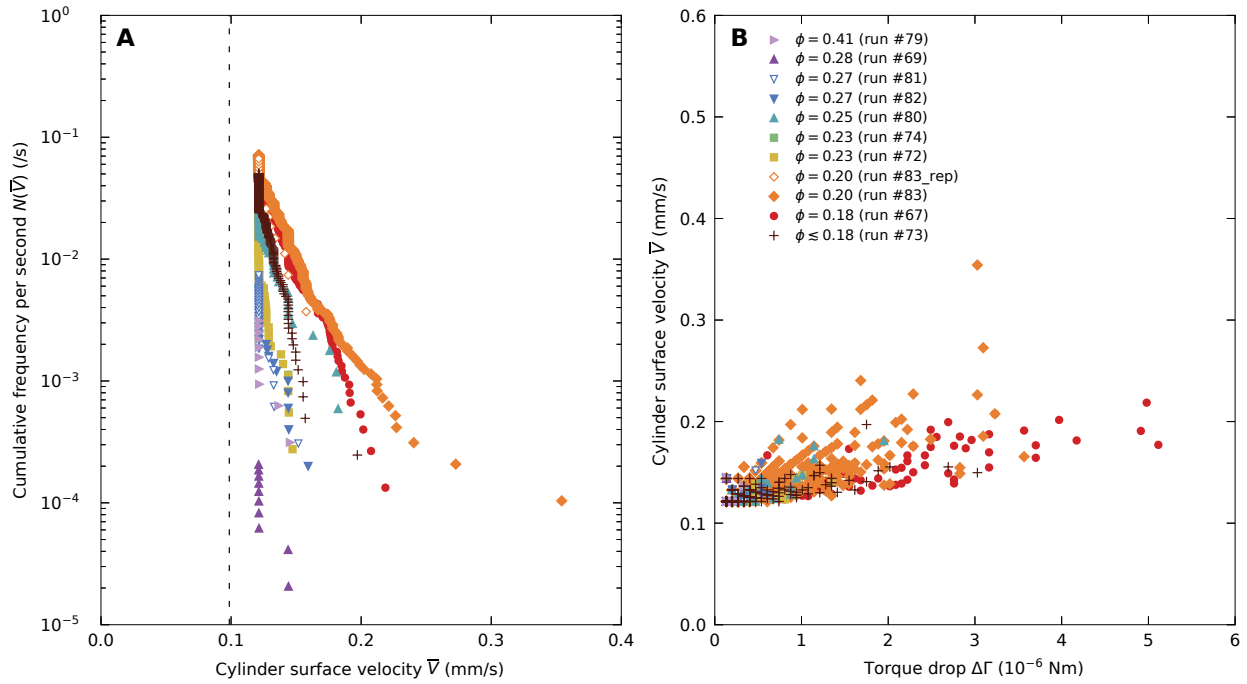


Figure S8: Slip velocity distribution as functions of porosity ϕ and torque drop amplitude $\Delta\Gamma$. The symbols and colors are common in all subplots. **(A)** Cumulative frequency distribution of the slip velocity \bar{V} on the surface of the cylinder. The dashed line indicates the constant motor velocity without any torque resistance. The resolution of the calculated velocity is approximately 0.02 mm/s in this experimental system. Symbols and colors are the same as **(B)**. **(B)** Torque drop dependence of the slip velocity.

Table S1: Experimental Conditions. Performed experimental run number, number of particles, porosity condition, analyzed run duration and detected event number are summarized as follows.

Run#	System size (mm)	Number of particles*	Porosity	Run duration (s)	Detected events
79	300	2746	0.41	3194	10
69	300	3314	0.28	48704	10
81	300	3368	0.27	3264	24
82	300	3368	0.27	4984	29
80	300	3474	0.25	1699	68
70 [†]	300	3514	0.24	184	0
74	300	3560	0.23	885	2
72	300	3614	0.22	3628	82
83	300	3690	0.20	9630	690
83rep [‡]	300	3690	0.20	267	18
67 [†]	300	3781	0.18	7512	466
73 [§]	300	3914	$\lesssim 0.18$	4052	204
30	100	401	0.26	16819	672
31 [¶]	100	411	0.24	63459	5103
29	100	421	0.22	72289	6493
28	100	441	0.18	12436	1130
27 [§]	100	461	$\lesssim 0.18$	65821	5941
87 [#]	300	4760	N/A	15725	1125

* Number of particles including 16 particles (17 for the 100 mm system) glued to the rotating cylinder.

[†] Particles intentionally arranged in an ordered polycrystal structure.

[‡] Performed at the end of run #83 to verify reproducibility.

[§] A small percentage of all particles out of the plane of the granular layer.

[¶] Including 10 particles without the immersion pretreatment.

[#] Using the glass beads with a diameter of 4.1 mm.

Caption for Movie S1. Representative time-series of the particle motions. An animated version is displayed for the binary image differences with a 2-second interval in run #83, including the images in Fig. 3B, D, and E. The white color shows the differences between the binary images with an interval of 2 s, indicating the areas swept by particles. The frame rate is 10 fps and the playback speed is the same as the actual speed. The playback time of 0, 337.7, 352.8, and 495.4 s corresponds to the run time of 1890.1, 2229.3, 2244.5, and 2387.8 s (the difference in brightness values is calculated between two images taken ± 1 s apart), respectively.